Magnetic properties of the triangular-lattice antiferromagnets $Ba_3RB_9O_{18}$ (R = Yb, Er)

J. Khatua,[1] M. Pregelj,[2,6] A. Elghandour,[3] Z. Jagličić,[4,5] R. Klingeler,[3] A. Zorko,[2,6] and P. Khuntia[1,7,8,*]

[1]*Department of Physics, Indian Institute of Technology Madras, Chennai 600036, India*
[2]*Jožef Stefan Institute, Jamova cesta 39, 1000 Ljubljana, Slovenia*
[3]*Kirchhoff Institute of Physics, Heidelberg University, INF 227, D-69120 Heidelberg, Germany*
[4]*Institute of Mathematics, Physics and Mechanics, Jadranska 19, 1000 Ljubljana, Slovenia*
[5]*Faculty of Civil and Geodetic Engineering, University of Ljubljana, Jamova 2, 1000 Ljubljana, Slovenia*
[6]*Faculty of Mathematics and Physics, University of Ljubljana, Jadranska ulica 19, 1000 Ljubljana, Slovenia*
[7]*Quantum Centre for Diamond and Emergent Materials, Indian Institute of Technology Madras, Chennai 600036, India*
[8]*Functional Oxide Research Group, Indian Institute of Technology Madras, Chennai 600036, India*

(Received 18 October 2021; revised 9 June 2022; accepted 22 August 2022; published 9 September 2022)

Frustration-induced strong quantum fluctuations, spin correlations, and interplay between competing degrees of freedom are some of the key ingredients that underlie exotic states with fractional excitations in quantum materials. Rare-earth-based two-dimensional magnetic lattices possessing a crystal electric field, spin-orbit coupling, anisotropy, and electron correlation between rare-earth moments offer a new paradigm in this context. Herein, we present crystal structure, magnetic susceptibility, and specific heat results accompanied by crystal electric field calculations on polycrystalline samples of $Ba_3RB_9O_{18}$ (R = Yb, Er), in which R^{3+} ions form a perfect triangular lattice. The localized R^{3+} spins show neither long-range magnetic order nor spin-glass behavior down to 1.9 K in $Ba_3RB_9O_{18}$. Magnetization data reveal pseudospin $J_{\text{eff}} = 1/2$ (Yb^{3+}) degrees of freedom in the Kramers doublet state and a weak antiferromagnetic interaction between $J_{\text{eff}} = 1/2$ moments in the Yb variant. On the other hand, the effective moment $\mu_{\text{eff}} = 8.8\ \mu_B$ was obtained from the Curie-Weiss fit of the low-temperature susceptibility data in $Ba_3ErB_9O_{18}$, which suggests the admixture of higher-crystal-electric-field states with the ground state. The Curie-Weiss fit of low-temperature susceptibility data for the Er system unveils the presence of a bit stronger antiferromagnetic interaction between Er^{3+} moments compared with its Yb^{3+} analog. $Ba_3ErB_9O_{18}$ does not show long-range magnetic order down to 500 mK. Furthermore, our crystal electric field calculations based on the thermodynamic data suggest the presence of a small gap between the ground and first excited Kramers doublets. The broad maximum around 4 K in the specific heat at zero field is attributed to the thermal population of the first crystal electric field excited state in $Ba_3ErB_9O_{18}$.

DOI: 10.1103/PhysRevB.106.104408

I. INTRODUCTION

Geometrically frustrated magnets, wherein magnetic ions are arranged on corner- or side-shared triangular motifs, have been of intense research interest [1,2]. In such materials, competing interactions accompanied by strong quantum fluctuations can lead to exotic ground states such as quantum spin liquids (QSLs) [3,4]. Quantum spin liquids are characterized by the absence of phase transitions down to $T \to 0$ despite strong exchange interaction between electron spins. In the QSL state, spins maintain a highly entangled state and support exotic fractional excitations that are essential ingredients for quantum computing [3–7]. Beyond the fundamental physics point of view, it has been generally believed that a high-T_c superconducting state can be realized from the parent QSL state since the seminal proposal of Anderson in 1973 [3,8].

The experimental realization of the QSL state in a frustrated magnet that is Cu^{2+} ($S = 1/2$) based—such as in the triangular lattice κ-$(ET)_2Cu_2(CN)_3$ [9], kagome lattice $ZnCu_3(OH)_6Cl_2$ [10,11], and hyperkagome lattice $PbCuTe_2O_6$ [12]—due to frustration-induced strong quantum fluctuations has generated a flurry of research activities in an effort to broaden our understanding of exotic fractional excitations in the entangled states of correlated quantum matter [1,9]. Especially, the $S = 1/2$ triangular-lattice antiferromagnet is one of the simplest two-dimensional prototypical frustrated quantum magnets that offers a versatile platform to observe remarkable quantum many-body phenomena, for example, QSLs in 1T-TaS_2 [13] and $Ba_3CuSb_2O_9$ [14], quantum magnetization and continuum excitations in $Ba_3CoSb_2O_9$ [15], and unconventional spin dynamics in an hourglass magnet [16]. Despite enormous efforts, ideal realizations of QSLs remain scarce due to antisite disorder, defects, and the presence of complex magnetic interactions in real quantum materials [17–19].

Recently, rare-earth-based triangular-lattice antiferromagnets in which anisotropic magnetic interactions are induced by spin-orbit coupling and the crystal electric field offer an alternate route to realize exotic quantum phenomena [20]. Similar to $4d$ and $5d$ systems [21], rare-earth magnets in which $4f$ shells are accommodated with an odd number

*pkhuntia@iitm.ac.in

of electrons can also host a low-energy effective 1/2 spin in the lowest Kramers doublet state [22]. For instance, the rare-earth magnet $YbMgGaO_4$, in which Yb^{3+} ions form a triangular lattice in the *ab* plane, shows promising quantum many-body phenomena [23,24]. The negative value of the Curie-Weiss temperature (approximately equal to −4 K) obtained from the fit of low-temperature magnetic susceptibility data suggests the presence of an antiferromagnetic interaction between $J_{\text{eff}} = 1/2$ moments in $YbMgGaO_4$. A power-law behavior of magnetic specific heat at low temperature suggests that $YbMgGaO_4$ is a gapless quantum-spin-liquid candidate [23]. Muon-spin relaxation measurement reveals that localized Yb^{3+} spins maintain a dynamic ground state down to 60 mK [25]. Also, the presence of fractionalized spinon excitations was suggested by inelastic neutron scattering experiments [26]. However, the presence of disorder due to Ga^{3+} and Mg^{2+} site sharing puts a strong constraint on the unambiguous identification of the ground state of $YbMgGaO_4$ [27,28]. Theoretically, it is suggested that the presence of intersite defects in the crystalline structure provides an additional source to destabilize long-range magnetic order by the randomized exchange interactions [29].

In this respect, rare-earth delafossite materials, $NaYbX_2$ (X = O, S, and Se), provide a promising venue to host spin-orbit-driven novel quantum states [30–33]. In delafossite materials, the nearest-neighbor Yb^{3+} ions (3.34 Å) are arranged on a triangular lattice without antisite disorder between constituent atoms, and the antiferromagnetic interaction between Yb^{3+} moments is a bit stronger compared with that in $YbMgGaO_4$. In addition, thermodynamic and muon-spin resonance experiments on $NaYbX_2$ reveal that Yb^{3+} spins do not undergo a magnetic long-range order down to 50 mK in zero magnetic field [33–35]. However, most of the Yb-based delafossite materials show a magnetization plateau and long-range magnetic order in the presence of an applied magnetic field that plays an important role in tuning the interplane interactions [31,33]. Electron-spin resonance measurements on single crystals of $NaYbX_2$ suggest the presence of an anisotropic magnetic interaction between Yb^{3+} spins [36,37]. Remarkably, a pressure-induced Mott transition followed by the emergence of superconductivity has been observed in the QSL candidate $NaYbSe_2$ [38]. A similar scenario of pressure-induced Mott transition and superconductivity is also observed in the organic-based QSL candidate κ-$(ET)_2Cu_2(CN)_3$ [39]. In addition to next-nearest-neighbor interaction, which melts 120° magnetic order [40,41], exchange anisotropy in Yb-based triangular-lattice antiferromagnets offers a novel route to stabilize the spin-liquid state [42,43].

Despite the large angular momentum, the Er ($4f^{11}$, $^4I_{15/2}$, $J = 15/2$) member of the rare-earth series is a potential candidate to host novel correlated quantum phenomena due to the interplay between frustration and exchange anisotropy, which is a very fundamental requirement to understand quantum effects in rare-earth materials at low temperature [44,45]. In rare-earth magnetic materials, the anisotropy originates from the combination of spin-orbit coupling, local symmetry of rare-earth sites, and anisotropic superexchange interaction. Similar to the Yb system, the ground state of the Er analog can host $J_{\text{eff}} = 1/2$ degrees of freedom due to the crystal electric field with either an XY or an Ising nature of exchange anisotropy at low temperature [44,46]. Er-based magnets, where the $^4I_{15/2}$ multiplet splits in the local crystal electric field environment into a Kramers doublet with the lowest energy for $J_{\text{eff}} = 1/2$, are ideal for hosting many anisotropy-driven ground states. For instance, the pyrochlore lattice $Er_2Ti_2O_7$ and triangular lattice $K_3Er(VO_4)_2$ exhibit XY anisotropy [47–49], while the triangular lattice $ErMgGaO_4$ and hyperkagome lattice $Er_3Ga_5O_{12}$ show strong Ising anisotropy [50–52]. Unlike $ErMgGaO_4$, the aforementioned Er based magnets undergo a phase transition at very low temperature. $ErMgGaO_4$ does not order down to 25 mK; however, it is not clear whether the randomness due to Mg^{2+} and Ga^{3+} antisite disorder leads to the disordered ground state in this antiferromagnet [29]. Recently, the Er member of the rare-earth delafossite series $AErC_2$ (A = Na, K, and Cs, and C = S, Se, and Te) is highlighted as a structurally ideal platform to explore spin-orbit-driven quantum many-body phenomena [53–57]. In the triangular lattice $KErS_2$, further-neighbor in-plane magnetic interaction and easy-plane anisotropy stabilize the antiferromagnetic ordered state below 0.2 K [54]. Although some rare-earth delafossites exhibit a magnetically ordered state at low temperature, these systems have still been of considerable research interest in recent years because they are promising candidates to host myriads of intriguing physical phenomena such as single-ion anisotropy, the coexistence of three-dimensional and quasi-two-dimensional order, reduced moment in the ordered state, the order-by-disorder state, and the transverse-field Ising model, to name a few [49,54,58,59]. The current interest is to investigate spin-orbit-driven frustrated magnets in a structurally perfect triangular lattice based on rare-earth ions for the experimental realization of novel states and to explore the ground-state properties under external perturbations in a controlled manner.

Herein, we report the crystal structure, magnetic susceptibility, and specific heat results along with crystal electric field calculations on an interesting class of rare-earth-based magnets, $Ba_3RB_9O_{18}$ (R = Yb, Er), where R^{3+} ions constitute a structurally perfect triangular lattice perpendicular to the c axis. In $Ba_3RB_9O_{18}$, the localized R^{3+} ions interact antiferromagnetically albeit weakly and exhibit neither long-range magnetic order nor a spin-glass state down to 1.9 K. Our results reveal a Kramers doublet state of Yb^{3+} spin with an effective low-energy state, $J_{\text{eff}} = 1/2$, at low temperature owing to the crystal electric field and spin-orbit coupling for the Yb triangular lattice. A relatively higher Curie-Weiss temperature indicates the presence of a bit stronger antiferromagnetic interaction between Er^{3+} moments in the triangular lattice $Ba_3ErB_9O_{18}$ compared with its Yb analog. Furthermore, the Er variant does not show a phase transition down to 500 mK as revealed by our magnetization measurements. The presence of a broad maximum around 4 K in the zero-field specific heat data of the Er triangular lattice suggests the presence of low-lying crystal field excitations due to a small gap between the two lowest Kramers doublet states.

II. EXPERIMENTAL DETAILS

Polycrystalline samples of $Ba_3RB_9O_{18}$ (R = Yb, Er) were prepared by a conventional solid-state reaction method. $BaCO_3$ (Alfa Aesar, 99.997%), R_2O_3 (Alfa Aesar, 99.998%),

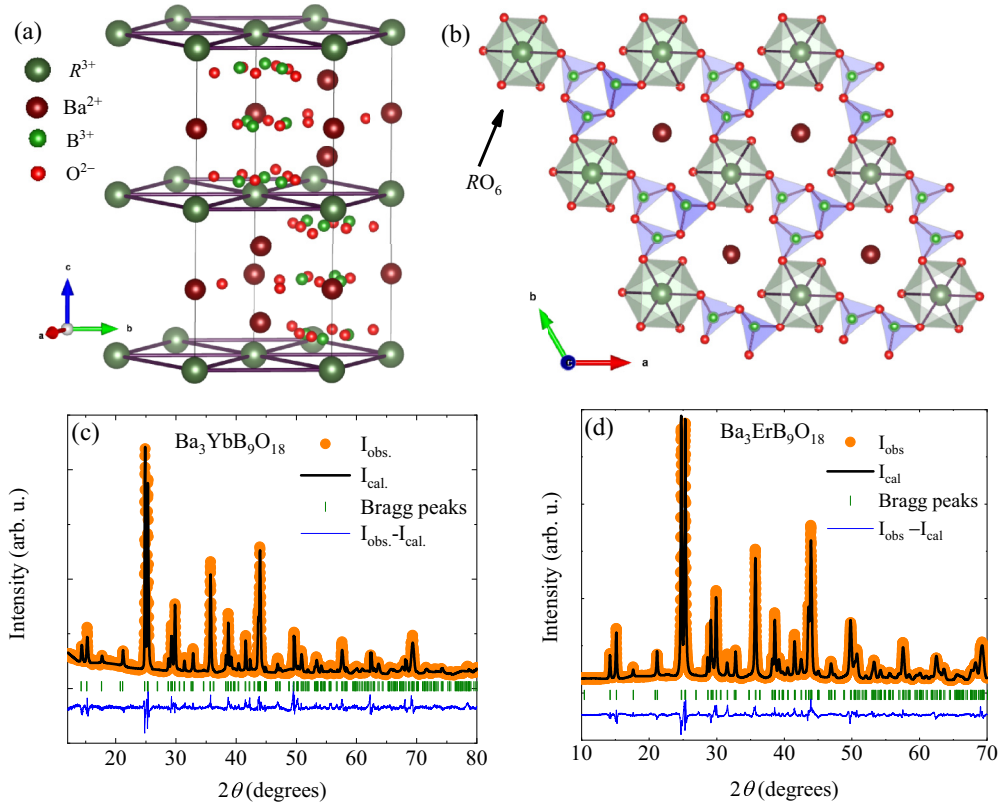

FIG. 1. (a) Schematic view of the crystal structure of $Ba_3RB_9O_{18}$ (R = Yb, Er), where the solid lines denote the boundary of the unit cell. R^{3+} ions form triangular lattices, which are stacked along the c axis with interplanar distance 8.44 Å. (b) RO_6 octahedra constituted by the nearest-neighbor oxygen ligand of R^{3+} ions. (c) The Rietveld refinement pattern of the room-temperature powder x-ray diffraction data of $Ba_3YbB_9O_{18}$. Experimentally observed points, the result of Rietveld fitting, expected Bragg reflection positions, and the difference between observed and calculated intensities are shown by the orange circles, black line, olive vertical bars, and blue line, respectively. (d) The Rietveld refinement pattern of the room-temperature powder x-ray diffraction data of $Ba_3ErB_9O_{18}$.

and H_3BO_3 (Alfa Aesar, 98%) were mixed in stoichiometric quantities, while 10% excess H_3BO_3 was used due to its volatile nature. The reagent R_2O_3 was preheated at 700 °C overnight to remove moisture and carbonates prior to use. The stoichiometric mixture was pelletized, and the pellet was loaded into a platinum crucible for sintering at 600 °C for 24 h. This sintering process was repeated at several intermediate temperatures, and finally a single phase was obtained by annealing the sample at 950 °C for 48 h. Powder x-ray diffraction (XRD) data of $Ba_3RB_9O_{18}$ were collected by employing a Panalytical X′Pert Pro powder diffractometer with Cu K_α radiation (λ = 1.54 Å) at room temperature. Magnetization measurements were performed using a Quantum Design superconducting quantum interference device with vibrating sample magnetometer (SQUID VSM) in the temperature range 5 K $\leqslant T \leqslant$ 340 K and in magnetic fields up to 7 T for $Ba_3YbB_9O_{18}$ (BYBO) samples. Magnetization measurements in the range 2 K $\leqslant T \leqslant$ 300 K in applied magnetic fields up to 5 T were performed using a Quantum Design MPMS XL-5 SQUID magnetometer using a closed-cycle cryostat for $Ba_3ErB_9O_{18}$ (BEBO) samples. Furthermore, low-temperature magnetization measurements down to 0.5 K were carried out using the ^{3}He option of the MPMS3 SQUID magnetometer from Quantum Design. Fitting and modeling of the crystal electric field (CEF) effects was performed using PHI software [60]. Specific heat measurements were performed using a Quantum Design physical properties measurement system (PPMS) in the temperature range 1.9 K $\leqslant T \leqslant$ 250 K and in magnetic fields up to 7 T.

III. RESULTS

A. Rietveld refinement and crystal structure of $Ba_3RB_9O_{18}$, R = (Yb, Er)

To confirm the phase purity, Rietveld refinement of x-ray diffraction data was performed using GSAS software [61]. We used the atomic coordinates of $Ba_3YB_9O_{18}$ as initial parameters to perform Rietveld refinement [62]. The result of the Rietveld refinement is shown in Figs. 1(c) and 1(d) for the Yb and Er variants, respectively. The obtained atomic parameters and goodness factors are summarized in Tables I and II and are in good agreement with earlier reports [62,63]. Both of the magnets, BYBO and BEBO, crystallize in the hexagonal structure with space group $P63/m$, where R^{3+} ions form a structurally perfect two-dimensional triangular lattice perpendicular to the c axis, as shown in Fig. 1(a). The absence of antisite disorder in these magnets compared with the well-studied rare-earth triangular-lattice antiferromagnets $YbMgGaO_4$ and $ErMgGaO_4$ suggests that $Ba_3RB_9O_{18}$ (R = Yb, Er) are promising candidates to explore quantum disordered states (Table III). The magnetic R^{3+} ion constitutes RO_6 octahedra with the nearest-neighbor oxygen ions.

TABLE I. Atomic coordinates of $Ba_3YbB_9O_{18}$ determined from the Rietveld refinement of x-ray diffraction data at 300 K (space group $P63/m$; $\alpha = \beta = 90.0^\circ$, $\gamma = 120.0^\circ$, $a = b = 7.169$ Å, $c = 16.895$ Å, and $\chi^2 = 4.22$; weighted profile residual $R_{wp} = 5.88\%$, profile residual $R_p = 3.39\%$, and expected profile residual $R_{exp} = 2.9\%$). Occ., occupation.

Atom	Wyckoff position	x	y	z	Occ.
Yb	$2b$	0	0	0	1
Ba_1	$4f$	0.666	0.333	0.1303	1
Ba_2	$2a$	0	0	0.25	1
B_1	$6h$	0.518	−0.1544	0.25	1
B_2	$12i$	−0.454	−0.314	0.076	1
O_1	$6h$	0.302	−0.165	0.25	1
O_2	$12i$	0.482	−0.139	0.079	1
O_3	$6h$	0.653	0.057	0.25	1
O_4	$12i$	−0.283	−0.266	0.085	1

Furthermore, in-plane RO_6 octahedra with equal Yb-O distance (2.509 Å) are connected through BO_3 triangles as shown in Fig. 1(b). One unit cell is composed of three triangular layers of R^{3+} ions with interplanar distance 8.44 Å, while the intraplane distance between R^{3+} ions is the length of the a axis, which is associated with the type of rare-earth ion. Structurally, the most striking difference of BYBO or BEBO with respect to $YbMgGaO_4$ and $NaYbO_2$ is that RO_6 octahedra are isolated in BRBO, whereas in $YbMgGaO_4$ and $NaYbO_2$, YbO_6 octahedra are connected with each other via a common oxygen ligand [23,33]. This difference possibly accounts for the modification of the strength of magnetic exchange interaction between Yb^{3+} moments as observed in the triangular lattice $KBaYb(BO_3)_2$ [64]. In $Ba_3RB_9O_{18}$, we observed that the lattice parameters of the Er triangular lattice are a bit larger compared with its Yb analog. This obvious structural modification in BEBO is expected owing to the different ionic radius of the Er^{3+} ion. Since there is no structural change, it is interesting to observe the impact of different R^{3+} ions within the same triangular motif on the magnetic properties.

TABLE II. Structural parameters of $Ba_3ErB_9O_{18}$ determined from the Rietveld refinement of x-ray diffraction data at 300 K (space group $P63/m$; $\alpha = \beta = 90.0^\circ$, $\gamma = 120.0^\circ$, $a = b = 7.19$ Å, $c = 17.01$ Å, and $\chi^2 = 3.8$; $R_{wp} = 6.5\%$, $R_p = 4.2\%$, and $R_{exp} = 3.33\%$).

Atom	Wyckoff position	x	y	z	Occ.
Er	$2b$	0	0	0	1
Ba_1	$4f$	0.666	0.333	0.131	1
Ba_2	$2a$	0	0	0.25	1
B_1	$6h$	0.503	−0.152	0.25	1
B_2	$12i$	−0.463	−0.266	0.073	1
O_1	$6h$	0.292	−0.173	0.25	1
O_2	$12i$	0.504	−0.117	0.083	1
O_3	$6h$	0.642	0.041	0.25	1
O_4	$12i$	−0.283	−0.271	0.089	1

B. Magnetic susceptibility

1. $Ba_3YbB_9O_{18}$

The temperature dependence of the magnetic susceptibility of BYBO in magnetic fields $\mu_0 H = 0.5$ and 1 T is shown in Fig. 2(a). The absence of any anomaly in the magnetic susceptibility [see Fig. 2(a)] suggests that Yb^{3+} moments do not undergo a long-range magnetic ordering down to 5 K. The absence of zero-field-cooled (ZFC) and field-cooled (FC) splitting of the magnetic susceptibility data [see inset of Fig. 2(a)] in 100 Oe rules out spin freezing in this magnet. The high-temperature susceptibility data follow the Curie-Weiss law, $\chi(T) = \chi_0 + C/(T - \theta_{CW})$, where χ_0 accounts for the contributions from temperature-independent core-diamagnetic and Van Vleck susceptibilities, C is the Curie constant, and θ_{CW} is the Curie-Weiss temperature representing a characteristic energy scale of interaction between the magnetic moments of the materials under study. The Curie-Weiss (CW) fit [Fig. 2(b)] of the magnetic susceptibility data in the temperature range 100 K $\leqslant T \leqslant$ 340 K yields an effective moment $\mu_{eff} = \sqrt{8C} = 4.73\ \mu_B$, which is comparable to that expected for free Yb^{3+} ions ($4f^{13}$, $^2F_{7/2}$), and $\theta_{CW} = -90$ K, which is attributed to the presence of a crystal electric field. The nature of Yb^{3+} spins is expected to be different at lower temperature due to an interplay between spin-orbit coupling and the crystal electric field. In principle, the correlation between $4f$ moments emerges at low temperature. In order to get a rough idea about the energy scale of interaction between $4f$ moments in BYBO, the magnetic susceptibility data were fitted with the Curie-Weiss law in the temperature range 5 K $\leqslant T \leqslant$ 15 K. The CW fit results in $\theta_{CW} = -0.12 \pm 0.02$ K and $\mu_{eff} = 2.32\ \mu_B$. The obtained effective moment ($2.32\ \mu_B$) is lower than the moment of free Yb^{3+} ions according to Hund's rule, which suggests that the crystal electric field leads to a Kramers doublet state of Yb^{3+} ions with a low-energy state, $J_{eff} = 1/2$, at low temperature. The small and negative value of θ_{CW} indicates the presence of a weak antiferromagnetic exchange interaction between Yb^{3+} moments.

The isotherm magnetization of BYBO is depicted in Fig. 2(c). The absence of a finite magnetic moment in zero field suggests that BYBO is free from ferromagnetic signal. The observed field dependence of the magnetization data is well captured [Fig. 2(c)] by $M/M_s = B_{1/2}(y)$, where $B_J(y) = [\frac{2J+1}{2J}\coth[\frac{y(2J+1)}{2J}] - \frac{1}{2J}\coth\frac{y}{2J}]$ is the Brillouin function, M_s ($= gJ\mu_B$) is the saturation magnetization, and $y = g\mu_B J\mu_0 H/k_B T$, with μ_B being the Bohr magneton and g being Landé's g factor. This fit yields powder-average Landé g factors 2.61 and 2.54 for 5 and 10 K, respectively, while J was fixed to 1/2. The effective magnetic moment $\mu_{eff} = 2.26\ \mu_B$ is obtained using $\mu_{eff} = g\mu_B\sqrt{J(J+1)}$, where $g = 2.61$ is known from the Brillouin function fit. The obtained Landé g factor from the Brillouin fit yields an effective moment expected for a low-energy state, $J_{eff} = 1/2$, which is close to that determined from the Curie-Weiss fit of the $1/\chi$ data.

2. $Ba_3ErB_9O_{18}$

To observe the variation of magnetic properties by introducing a different rare-earth ion in the isostructural

TABLE III. Some promising rare-earth-based frustrated triangular-lattice antiferromagnets with their ground-state properties.

Material (symmetry)	θ_{CW} (K) High T	θ_{CW} (K) Low T	μ_{eff} (μ_B) High T	μ_{eff} (μ_B) Low T	Anisotropy	Δ(CEF) (K)	T_N (K)	Ref.
$YbMgGaO_4$ ($R\bar{3}m$)		−4		2.8	Heisenberg	440		[23,65]
$NaYbO_2$ ($R\bar{3}m$)	−100	−5.6	4.54	2.84	XY	404		[35]
$NaYbS_2$ ($R\bar{3}m$)	−65	−4.5	4.5	2.8	XY	266		[31]
$NaYbSe_2$ ($R\bar{3}m$)	−66	−7	4.5	2.43	XY	183		[32,66]
$NaBaYb(BO_3)_2$ ($R\bar{3}m1$)	−113	−0.069	4.64	2.23				[67]
$Rb_3Yb(PO_4)_2$ ($P\bar{3}m1$)	−93	−0.05	4.66	2.23				[68]
$NdTa_7O_{19}$ ($P\bar{6}c2$)	−78	−0.46	3.8	1.9	Ising	110		[20]
$Ba_3YbB_9O_{18}$ (P63/m)	**−90**	**−0.12**	**4.73**	**2.32**				**This work**
$K_3Er(VO_4)_2$ (C2/c)		−3			XY		0.15	[49]
$NaErSe_2$ ($R\bar{3}m$)	−10.9	−4.3	9.5	9.4	XY			[53,55,57]
$KErSe_2$ ($R\bar{3}m$)	−8	−3.8	9.5	9.4	XY	10.6	0.2	[53,54,57]
$ErMgGaO_4$ ($R\bar{3}m$)	−33	−3.9	9.5	7	Ising			[50,52]
$Ba_3ErB_9O_{18}$ (P63/m)	**−1**	**−0.2**	**10.58**	**8.8**		**9.15**		**This work**

compound, we have measured the temperature dependence of the magnetic susceptibility of BEBO in various applied magnetic fields. Figure 3(a) depicts the temperature dependence of the magnetic susceptibility of BEBO in different magnetic fields. Our magnetic susceptibility data do not exhibit any signature of a phase transition down to 500 mK. Magnetic susceptibility χ was measured in 0.1 T in the ZFC and FC regimes [inset of Fig. 3(a)]. The two data sets exactly coincide, implying the absence of potential spin freezing. The inverse susceptibility $1/\chi$ exhibits almost perfect linear temperature dependence, which can be fitted [red line in Fig. 3(b)] to the Curie-Weiss law yielding Curie-Weiss temperature $\theta = -1.0(1)$ K for temperatures greater then 150 K. Concerning the Curie-Weiss fit at low temperatures, θ_{CW} is obviously highly dependent on the fitting range. Hence we have performed the fitting with the Curie-Weiss model in the low-temperature range systematically by varying the upper temperature limit of the fitting range, T_{max}, as done in Ref. [20], which is presented in the inset of Fig. 3(b). The results of our analysis clearly suggest that θ_{CW} is highly

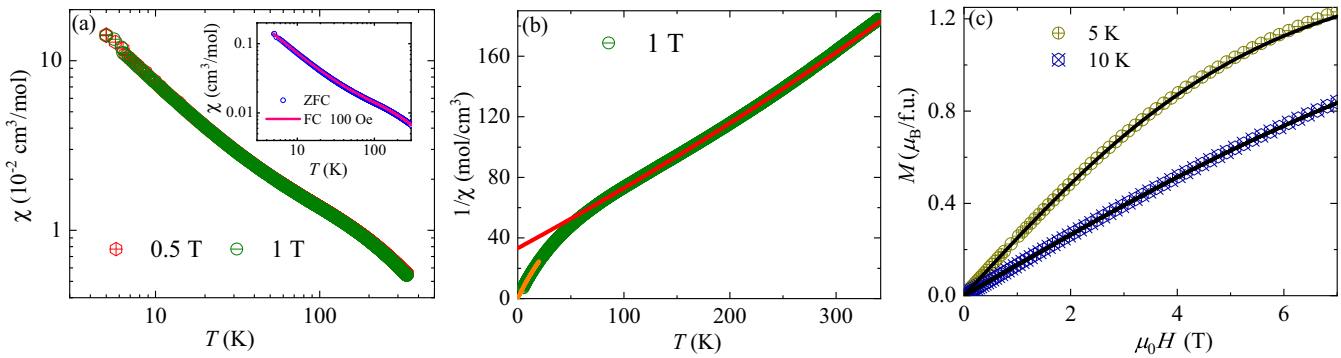

FIG. 2. (a) The temperature dependence of magnetic susceptibility, $\chi(T)$, of BYBO in two different magnetic fields. The inset shows the temperature dependence of the zero-field-cooled (ZFC) and field-cooled (FC) magnetic susceptibility measured in $H = 100$ Oe. (b) The temperature dependence of inverse magnetic susceptibility. The red and orange lines represent the Curie-Weiss fits to the high-temperature and low-temperature inverse susceptibility data, respectively. (c) Magnetization as a function of external magnetic field at 5 and 10 K; the solid lines are the Brillouin function fit of paramagnetic Yb^{3+} ions.

TABLE IV. CEF parameters (in meV) for CEF Hamiltonian of Eq. (1), g factors of the ground state, and sum of squares $\sum = \prod_{k=1}^{\text{data sets}} [\sum_{i=1}^{k\text{ points}} (x_{k,\text{expt}} - x_{k,\text{calc}})^2]$ for the two competing CEF models.

Model	B_2^0	B_4^0	B_4^3	B_4^{-3}	B_6^0	B_6^3	B_6^{-3}	B_6^6	B_6^{-6}	g_x	g_y	g_z	$\sum$
Easy axis	133.03	42.42	534.73	135.51	12.83	−32.32	−15.22	24.66	8.82	3.143	3.143	7.770	0.00824
Easy plane	−93.14	22.54	189.16	95.90	−0.851	8.83	−28.02	32.86	113.19	2.086	6.575	6.575	0.0159

sensitive to the upper limit of the fitting range, as θ_{CW} gradually decreases when lowering T_{max}. Yet, below T_{max} of 0.75 K, θ_{CW} saturates at $\theta_{\text{CW}} \approx -0.2$ K, which thus reflects the actual interaction strength in the ground state of $Ba_3ErB_9O_{18}$.

In order to quantify the CEF effects, we performed additional susceptibility measurements in higher magnetic fields, i.e., at 1 and 5 T [Fig. 3(d)], as well as magnetization measurements at several temperatures [Fig. 3(c)]. Considering that the exchange interaction is probably of the order of 0.2 K, we performed a combined fit of all the magnetization and susceptibility data for temperatures greater than 5 K, i.e., approximately an order of magnitude greater than the expected exchange interaction. According to Hund's rule, the ground state multiplet of the Er^{3+} ion is $^4I_{15/2}$, which is in a crystal field split into eight Kramers doublets composed of $|\pm m_J\rangle$ states [m_J=(2n − 1)/2, where n = 1–8]. The composition of the eight Kramers doublets directly depends on the CEF

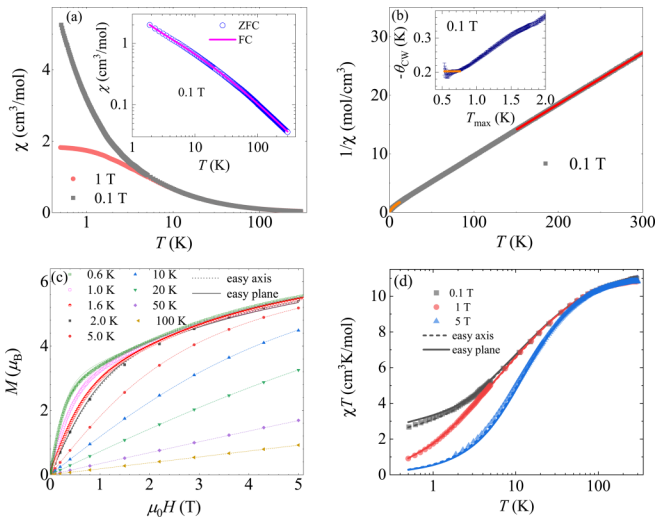

FIG. 3. (a) The temperature dependence of the magnetic susceptibility χ of BEBO in different magnetic fields down to 500 mK. The inset shows the temperature dependence of zero-field-cooled (ZFC) and field-cooled (FC) magnetic susceptibility measured in 0.1 T. (b) The temperature dependence of the inverse magnetic susceptibility, where red and orange lines are the Curie-Weiss fit to the high-temperature and low-temperature data, respectively. The inset depicts the dependence of the Curie-Weiss temperature θ_{CW} obtained following the Curie-Weiss model in the low-temperature range systematically by varying the upper temperature limit of the fitting range, T_{max}. (c) Magnetization as a function of the external magnetic field at several temperatures. (d) The temperature dependence of χT emphasizing the behavior of χ at low temperatures. Lines in (c) and (d) correspond to the two CEF models as described in the text (only data for $T \geqslant 5$ K were fitted).

Hamiltonian, which can be written as

$$H_{\text{CEF}} = \sum_{i,j} B_j^i O_j^i, \tag{1}$$

where O_j^i are Stevens operators [69] and B_j^i are the corresponding scaling parameters. The relevant B_j^i (Table IV) are determined by point symmetry at the Er^{3+} site. Indeed, we obtained a very good agreement with the data [lines in Figs. 3(c) and 3(d)], but the fitting does not yield a unique solution. In fact, two sets of CEF parameters (Table IV) both describe the data very well; yet they exhibit different magnetic ground states—an easy-axis solution and an easy-plane solution [dotted and solid lines in Figs. 3(c) and 3(d), respectively]. Moreover, both models yield similar energy levels for the lower CEF states (Table V), making the two solutions rather difficult to distinguish. Nevertheless, considering that the sum of squares [60] of the fit is smaller, by a factor of 2, for the easy-axis solution, we favor this solution over the easy-plane one. Finally, we note that small deviations of the calculated CEF responses at the lowest temperatures [Figs. 3(c) and 3(d)] are likely due to small but finite exchange interaction. We stress again that only data above 5 K were fitted. Future low-temperature heat capacity and muon experiments below 500 mK may reveal interesting cooperative quantum phenomena in this promising magnet.

C. Specific heat

1. $Ba_3YbB_9O_{18}$

Specific heat studies are ideal to understand the ground-state properties of the rare-earth triangular-lattice antiferromagnets $Ba_3RB_9O_{18}$ (R = Yb, Er). Figure 4(a) depicts the temperature dependence of the total specific heat, $C_p(T)$, of BYBO measured in zero field down to 1.9 K. The absence of an anomaly in the specific heat indicates that Yb^{3+} spins do not undergo a long-range magnetic ordering, at least not in the measured temperature range. The measured specific heat is the sum of magnetic specific heat due to localized Yb^{3+} spins and lattice specific heat due to phonon contributions. The magnetic specific heat $C_{\text{mag}}(T)$ provides information concerning correlated magnetic phenomena and degeneracy of the ground state. Therefore, to extract the magnetic specific heat, the lattice contribution was estimated by fitting the

TABLE V. CEF energy levels (in meV) for the two competing CEF models.

Model	E_0	E_1	E_2	E_3	E_4	E_5	E_6	E_7
Easy axis	0	1.13	3.12	9.21	48.47	48.97	56.66	127.70
Easy plane	0	1.28	4.51	12.34	20.08	60.62	65.33	69.67

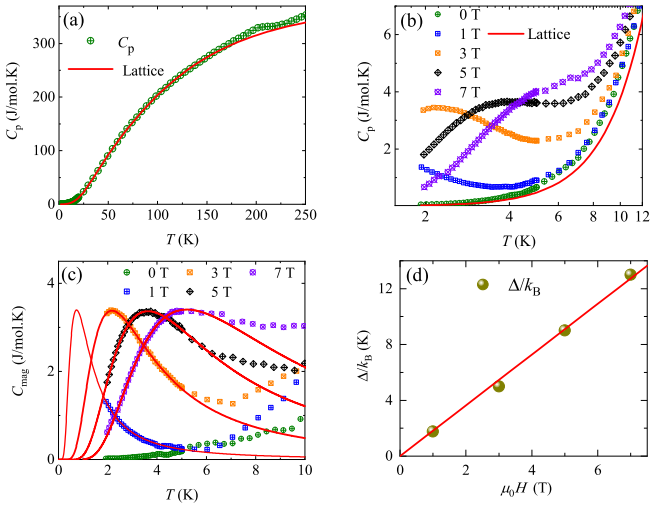

FIG. 4. (a) The temperature dependence of the specific heat C_p of BYBO in the temperature range 1.9 K $\leqslant T \leqslant$ 250 K in zero magnetic field; the solid line is the fit to two Debye functions used to extract the magnetic specific heat. (b) The temperature dependence of $C_p(T)$ in various magnetic fields. (c) The temperature dependence of $C_{\rm mag}(T)$, where the solid red lines are the expected Schottky contribution, i.e., Eq. (2), due to Zeeman splitting of the lowest Kramers doublet state. (d) The evolution of the gap with external magnetic field; the solid line represents a linear fit.

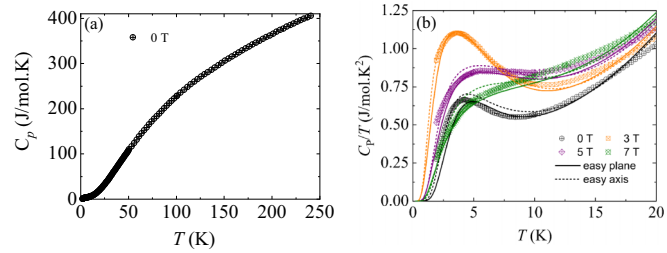

FIG. 5. (a) The temperature dependence of the specific heat C_p of BEBO in the temperature range 1.9 K $\leqslant T \leqslant$ 240 K in zero field. (b) Temperature dependence of C_p/T in various magnetic fields; the lines depict the fitted curves based on the two CEF models and an additional T^3 term accounting for the lattice contribution as described in the text.

experimental data with two Debye functions, i.e., $C_{\rm lat}(T) = 9k_{\rm B}[\sum_{n=1}^{2} C_n(\frac{T}{\theta_{D_n}})^3 \int_0^{\theta_{D_n}/T} \frac{x^4 e^x}{(e^x-1)^2} dx]$, where k_B is the Boltzmann constant, θ_{D_n} $(n = 1, 2)$ are Debye temperatures, and C_n are the coefficients. As shown in Fig. 4(a), in the temperature range 20 K $\leqslant T \leqslant$ 150 K, the experimentally observed $C_p(T)$ data can be well reproduced by the Debye model representing lattice specific heat with $\theta_{D_1} = 230$ K and $\theta_{D_2} = 345$ K. In this fit, the coefficients C_n were fixed in the ratio $C_1 : C_2 = 1 : 1.4$, which is the ratio of the total number of heavy atoms (Ba, Yb, and B) to the total number of light atoms (O) [70,71].

In order to gain further insight into the Kramers doublet state of Yb^{3+} ions, specific heat measurements were performed in several magnetic fields, and the results are presented in Fig. 4(b). It is observed that in the presence of a magnetic field, the temperature dependence of the C_p data exhibit a broad maximum. The specific heat starts increasing below 4 K in a 1 T magnetic field, which probably suggests a broad maximum at much lower temperatures. The broad maximum shifts towards higher temperature with increasing magnetic field. This scenario is attributed to the Zeeman splitting of the lowest Kramers doublet state [23].

The magnetic specific heat was obtained after subtracting the lattice specific heat from the total specific heat data and is shown in Fig. 4(c). Next, we fitted the high-field magnetic specific heat data below 10 K to the two-level Schottky anomaly [72]

$$C_{\rm Sch} = fR\left(\frac{\Delta}{k_B T}\right)^2 \frac{\exp(\Delta/k_B T)}{(1+\exp(\Delta/k_B T))^2}, \qquad (2)$$

where Δ is the gap of the Zeeman splitting of the ground-state Kramers doublet of Yb^{3+} ion, k_B is the Boltzmann constant, R is the universal gas constant, and f measures the fraction of electron spin which contributes to the splitting of the ground-state doublet. The best fit was achieved with $\Delta/k_B = 1.66$, 4.88, 9, and 13 K for a magnetic field of 1, 3, 5, and 7 T, respectively, as shown in Fig. 4(c). Also, the estimated fraction of spin, f, is $\geqslant$93%, which illustrates the good reproducibility of the $C_{\rm mag}(T)$ data as this fraction is close to 1. It is worth mentioning here that this fraction does not measure the fraction of defect spins or orphan spins, which are normally found in the range 5–10% due to defects in some disordered spin lattices. In $Ba_3YbB_9O_{18}$, the Schottky-like anomaly in the temperature dependence of the magnetic specific heat $C_{\rm mag}$ is of magnetic origin due to magnetic Yb^{3+} ions. Figure 4(d) depicts the evolution of the gap, i.e., $\Delta/k_{\rm B}$, with magnetic field, where the red line is the linear fit which yields $g = 2.69 \pm 0.04$ [72]. This value of g is close to that obtained from the analysis of the magnetization data reflecting the consistency of our results and the accuracy of the fitting parameters obtained from the two experiments.

2. $Ba_3ErB_9O_{18}$

Figure 5(a) represents the specific heat $C_p(T)$ of BEBO in zero field down to 1.9 K. For the clear visualization of low-temperature heat capacity data, the temperature dependence of C_p/T in several magnetic fields is shown in Fig. 5(b). It is apparent that there is no sharp anomaly down to 1.9 K suggesting the absence of long-range antiferromagnetic order of Er^{3+} moments. Rather, the zero-field specific heat data exhibit a broad maximum $T_{\rm max} \approx 4$ K suggesting the presence of low-lying crystal field excitations, which is also observed in several rare-earth-based frustrated triangular-lattice antiferromagnets [53,73–75].

Indeed, the sum of magnetic specific heat contributions calculated for the CEF parameters in Table IV (using the program PHI), $C_{\rm mag}$, and the phonon contribution that is at low temperatures proportional to T^3, i.e., $C_p = C_{\rm mag} + aT^3$, describes the observed behavior rather well [lines in Fig. 5(b)]. We note that $C_{\rm mag}$ was scaled by 0.85 to get a better agreement with the experiment. Still, the two models yield similar results, making it rather difficult to choose a favorable one. Nevertheless, the good agreement with the experiment rather suggests that there is most likely no magnetic specific heat at low temperatures.

IV. DISCUSSION

Frustrated triangular-lattice antiferromagnets offer an emblematic model for the experimental realization of novel quantum states with exotic excitations. Rare-earth magnets where $4f$ shells are occupied with an odd number of electrons can host effective $1/2$ moments which combine spin and orbital moments in the Kramers doublet state. One may expect such a $J_{\text{eff}} = 1/2$ moment of Yb^{3+} ions in BYBO (Yb^{3+}, $4f^{13}$) wherein the crystal electric field splits the spin-orbit-induced $2J + 1 = 8$ degenerate ground state ($^2J_{7/2}$) into four Kramers doublets. Indeed, the estimated effective moment $\mu_{\text{eff}} = 2.32\ \mu_B$ obtained from the magnetic susceptibility data suggests the formation of a Kramers doublet state in BYBO below 10 K. The small and negative Curie-Weiss temperature obtained from the fit of the low-temperature susceptibility data indicates the presence of a weak antiferromagnetic interaction between $J_{\text{eff}} = 1/2$ moments of Yb^{3+} ions. In some rare-earth magnets, the magnetic interaction is governed by dipolar and superexchange interaction despite strong localization of $4f$ electrons [76,77]. For instance, in $YbMgGaO_4$, the nearest-neighbor dipolar interaction between intralayer (3.4 Å) Yb^{3+} moments is of the order of 0.16 K, which is 11% of the nearest-neighbor exchange interaction, 1.36 K, that is estimated from the Curie-Weiss temperature [24]. This suggests that the dominant exchange energy in $YbMgGaO_4$ is due to antiferromagnetic superexchange interaction via Yb^{3+}-O^{2-}-Yb^{3+} virtual electron hopping processes [78]. In contrast, in BYBO, the intraplanar distance of the Yb^{3+} ion is 7.16 Å, which is almost double the intraplanar distance in $YbMgGaO_4$, which suggests the presence of a weak magnetic dipole-dipole interaction. The calculated dipole-dipole interaction in BYBO, following a phenomenological expression, $E_{\text{dip}} \approx \mu_0 g_{\text{av}}^2 \mu_B^2 / 4\pi a^3$ (where g_{av} is the powder-average Landé g factor and a is the nearest-neighbor Yb-Yb distance), is ∼0.011 K, which is 28% of the nearest-neighbor exchange interaction 0.04 K that is estimated from the Curie-Weiss temperature [24,79]. Therefore, in BYBO, superexchange interaction is weak as expected due to the presence of isolated YbO_6 octahedra that connect the intraplane YbO_6 octahedra via the virtual exchange path Yb-B-O-B-Yb. A similar scenario of low exchange interaction is observed in another rare-earth-based triangular lattice, $KBaYb(BO_3)_2$, where intraplane YbO_6 octahedra are not connected via common O^{2-} ions but rather separated spatially within the *ab* plane by BO_3 triangles [64]. In view of this, it is suggested that superexchange interaction is the main mechanism for magnetic coupling in the present Yb-based triangular lattice [80]. The specific heat data reveal the absence of magnetic order down to 1.9 K. In high magnetic field, the specific heat data exhibit a broad maximum which shifts to higher temperatures with increasing magnetic field. The shift of the broad maximum in C_m is attributed to the Zeeman splitting of the lowest Kramers doublet state of BYBO as observed in a few frustrated rare-earth magnets [81]. It is important to note here that the gap is proportional to the applied field and it yields a g factor which is in agreement with that obtained from the analysis of magnetic susceptibility [76].

In $Ba_3ErB_9O_{18}$, the reduction in the Er^{3+} moment (Er^{3+}, $4f^{11}$) suggests that the local symmetry of Er^{3+} could split the $2J + 1$ ($J = 15/2$) multiplet into Kramers doublets. We obtained a Curie-Weiss temperature of -0.2 K, which suggests the presence of a weak antiferromagnetic superexchange interaction between Er^{3+} moments in BEBO. In contrast to BYBO, we observed a broad maximum in specific heat data of BEBO in zero field that is attributed to crystal field excitations. This is further supported by our CEF calculations. The difference in the magnetic properties of BYBO and BEBO seems mainly due to different CEF effects, slight differences in bond length, and dipolar interactions. In BEBO, the dipolar interaction between Er^{3+} moments is expected to be larger due to the larger magnetic moment of Er^{3+} (8.8 μ_B) ions. In addition, the exchange interaction is associated with the nature of angular momentum states in the ground state [80]. Therefore, one can expect the strength of the exchange interaction to be different due to dissimilar anisotropies in the materials studied in this work. Despite there being very similar superexchange pathways in the investigated magnets, it is observed that in BEBO the in-plane superexchange path length is reduced by only 8.29×10^{-3} Å compared with its Yb analog as expected due to the ionic radius of the Er^{3+} ion being a bit larger. In order to find why the Curie-Weiss temperature in BEBO is a bit stronger than that in its Yb analog, we have calculated the dipolar interaction between Er^{3+} moments in BEBO using the powder-average Landé factor obtained from our CEF analysis as presented in Table IV. The calculated dipolar interaction in BEBO is found to be approximately five times larger than that found in BYBO [76,82]. Low-temperature thermodynamic and local probe measurements in $Ba_3RB_9O_{18}$ may reveal the nature of magnetic anisotropy. It is worthwhile to explore the role of rare-earth magnetic ions and anisotropy in the underlying magnetism and spin dynamics of this family of rare-earth-based triangular-lattice antiferromagnets. This may be highly relevant for establishing paradigmatic theoretical models to understand a large class of frustrated materials wherein exotic ground-state properties are born out of the intertwining of the crystal electric field, spin-orbit coupling, and electron correlations.

V. SUMMARY

In summary, we have synthesized and carried out magnetization and specific heat studies on a class of rare-earth based magnets, $Ba_3RB_9O_{18}$ (R = Yb, Er). The present family of compounds represents a structurally perfect magnet in which R^{3+} ions constitute a two-dimensional triangular lattice. The investigated R-based triangular-lattice antiferromagnets exhibit neither the signature of long-range magnetic ordering nor spin-glass behavior down to 500 mK. Magnetic susceptibility data of the Yb member of the family reveal the presence of a Kramers doublet of Yb^{3+} ions with an effective low-energy $J_{\text{eff}} = 1/2$ state and a weak antiferromagnetic interaction between $J_{\text{eff}} = 1/2$ moments. We found a broad maximum around 4 K in the zero-field specific heat in the Er analog BEBO owing to the crystal field excitations, which is consistent with the presence of a relatively small gap between the two lowest Kramers doublet states as reflected in our CEF calculations. The characteristic energy scale of interaction between Er^{3+} moments is weak, which is typical for rare-earth-based frustrated triangular-lattice antiferromagnets. The

present family of rare-earth triangular-lattice antiferromagnets offers a promising platform to realize frustration-driven quantum phenomena given the two-dimensional nature of the spin lattice and the presence of spin-orbit interaction. Microscopic experimental techniques such as neutron scattering and muon-spin relaxation experiments and theoretical calculations are desired to explore the ground-state properties and associated excitations driven by spin-orbit interactions, crystal electric field, and electron correlations in this class of rare-earth-based triangular-lattice antiferromagnets.

ACKNOWLEDGMENTS

P.K. acknowledges the funding by the Science and Engineering Research Board and the Department of Science and Technology, India, through research grants.

[1] L. Balents, Nature (London) **464**, 199 (2010).
[2] P. Khuntia, J. Magn. Magn. Mater. **489**, 165435 (2019).
[3] P. W. Anderson, Mater. Res. Bull. **8**, 153 (1973).
[4] *Introduction to Frustrated Magnetism: Materials, Experiments, Theory*, edited by C. Lacroix, P. Mendels, and F. Mila, Springer Series in Solid-State Sciences Vol. 164 (Springer, New York, 2011).
[5] L. Savary and L. Balents, Rep. Prog. Phys. **80**, 016502 (2017).
[6] C. Broholm, R. J. Cava, S. A. Kivelson, D. G. Nocera, M. R. Norman, and T. Senthil, Science **367**, eaay0668 (2020).
[7] C. Nayak, S. H. Simon, A. Stern, M. Freedman, and S. Das Sarma, Rev. Mod. Phys. **80**, 1083 (2008).
[8] P. A. Lee, N. Nagaosa, and X.-G. Wen, Rev. Mod. Phys. **78**, 17 (2006).
[9] Y. Zhou, K. Kanoda, and T.-K. Ng, Rev. Mod. Phys. **89**, 025003 (2017).
[10] P. Khuntia, M. Velazquez, Q. Barthélemy, F. Bert, E. Kermarrec, A. Legros, B. Bernu, L. Messio, A. Zorko, and P. Mendels, Nat. Phys. **16**, 469 (2020).
[11] T.-H. Han, J. S. Helton, S. Chu, D. G. Nocera, J. A. Rodriguez-Rivera, C. Broholm, and Y. S. Lee, Nature (London) **492**, 406 (2012).
[12] P. Khuntia, F. Bert, P. Mendels, B. Koteswararao, A. V. Mahajan, M. Baenitz, F. C. Chou, C. Baines, A. Amato, and Y. Furukawa, Phys. Rev. Lett. **116**, 107203 (2016).
[13] M. Klanjšek, A. Zorko, R. Žitko, J. Mravlje, Z. Jagličić, P. K. Biswas, P. Prelovšek, D. Mihailovic, and D. Arčon, Nat. Phys. **13**, 1130 (2017).
[14] J. A. Quilliam, F. Bert, E. Kermarrec, C. Payen, C. Guillot-Deudon, P. Bonville, C. Baines, H. Luetkens, and P. Mendels, Phys. Rev. Lett. **109**, 117203 (2012).
[15] S. Ito, N. Kurita, H. Tanaka, S. Ohira-Kawamura, K. Nakajima, S. Itoh, K. Kuwahara, and K. Kakurai, Nat. Commun. **8**, 235 (2017).
[16] R. Nath, A. A. Tsirlin, P. Khuntia, O. Janson, T. Förster, M. Padmanabhan, J. Li, Y. Skourski, M. Baenitz, H. Rosner, and I. Rousochatzakis, Phys. Rev. B **87**, 214417 (2013).
[17] P. Khuntia, R. Kumar, A. V. Mahajan, M. Baenitz, and Y. Furukawa, Phys. Rev. B **93**, 140408(R) (2016).
[18] M. R. Cantarino, R. P. Amaral, R. S. Freitas, J. C. R. Araújo, R. Lora-Serrano, H. Luetkens, C. Baines, S. Bräuninger, V. Grinenko, R. Sarkar, H. H. Klauss, E. C. Andrade, and F. A. Garcia, Phys. Rev. B **99**, 054412 (2019).
[19] R. Kumar, P. Khuntia, D. Sheptyakov, P. G. Freeman, H. M. Rønnow, B. Koteswararao, M. Baenitz, M. Jeong, and A. V. Mahajan, Phys. Rev. B **92**, 180411(R) (2015).
[20] T. Arh, B. Sana, M. Pregelj, P. Khuntia, Z. Jagličić, M. D. Le, P. K. Biswas, P. Manuel, L. Mangin-Thro, A. Ozarowski, and A. Zorko, Nat. Mater. **21**, 416 (2022).
[21] H. Takagi, T. Takayama, G. Jackeli, G. Khaliullin, and S. E. Nagler, Nat. Rev. Phys. **1**, 264 (2019).
[22] J. Khatua, S. Bhattacharya, Q. P. Ding, S. Vrtnik, A. M. Strydom, N. P. Butch, H. Luetkens, E. Kermarrec, M. S. Ramachandra Rao, A. Zorko, Y. Furukawa, and P. Khuntia, Phys. Rev. B **106**, 104404 (2022).
[23] Y. Li, H. Liao, Z. Zhang, S. Li, F. Jin, L. Ling, L. Zhang, Y. Zou, L. Pi, Z. Yang, J. Wang, Z. Wu, and Q. Zhang, Sci. Rep. **5**, 16419 (2015).
[24] Y. Li, Adv. Quantum Technol. **2**, 1900089 (2019).
[25] Y. Li, D. Adroja, P. K. Biswas, P. J. Baker, Q. Zhang, J. Liu, A. A. Tsirlin, P. Gegenwart, and Q. Zhang, Phys. Rev. Lett. **117**, 097201 (2016).
[26] Y. Shen, Y.-D. Li, H. Wo, Y. Li, S. Shen, B. Pan, Q. Wang, H. C. Walker, P. Steffens, M. Boehm, Y. Hao, D. L. Quintero-Castro, L. W. Harriger, M. D. Frontzek, L. Hao, S. Meng, Q. Zhang, G. Chen, and J. Zhao, Nature (London) **540**, 559 (2016).
[27] Z. Ma, J. Wang, Z.-Y. Dong, J. Zhang, S. Li, S.-H. Zheng, Y. Yu, W. Wang, L. Che, K. Ran, S. Bao, Z. Cai, P. Čermák, A. Schneidewind, S. Yano, J. S. Gardner, X. Lu, S.-L. Yu, J.-M. Liu, S. Li *et al.*, Phys. Rev. Lett. **120**, 087201 (2018).
[28] Y. Xu, J. Zhang, Y. S. Li, Y. J. Yu, X. C. Hong, Q. M. Zhang, and S. Y. Li, Phys. Rev. Lett. **117**, 267202 (2016).
[29] Z. Zhu, P. A. Maksimov, S. R. White, and A. L. Chernyshev, Phys. Rev. Lett. **119**, 157201 (2017).
[30] W. Liu, Z. Zhang, J. Ji, Y. Liu, J. Li, X. Wang, H. Lei, G. Chen, and Q. Zhang, Chin. Phys. Lett. **35**, 117501 (2018).
[31] M. Baenitz, P. Schlender, J. Sichelschmidt, Y. A. Onykiienko, Z. Zangeneh, K. M. Ranjith, R. Sarkar, L. Hozoi, H. C. Walker, J. C. Orain, H. Yasuoka, J. van den Brink, H. H. Klauss, D. S. Inosov, and T. Doert, Phys. Rev. B **98**, 220409(R) (2018).
[32] K. M. Ranjith, S. Luther, T. Reimann, B. Schmidt, P. Schlender, J. Sichelschmidt, H. Yasuoka, A. M. Strydom, Y. Skourski, J. Wosnitza, H. Kühne, T. Doert, and M. Baenitz, Phys. Rev. B **100**, 224417 (2019).
[33] M. M. Bordelon, E. Kenney, C. Liu, T. Hogan, L. Posthuma, M. Kavand, Y. Lyu, M. Sherwin, N. P. Butch, C. Brown, M. J. Graf, L. Balents, and S. D. Wilson, Nat. Phys. **15**, 1058 (2019).
[34] R. Sarkar, P. Schlender, V. Grinenko, E. Haeussler, P. J. Baker, T. Doert, and H.-H. Klauss, Phys. Rev. B **100**, 241116(R) (2019).
[35] L. Ding, P. Manuel, S. Bachus, F. Grußler, P. Gegenwart, J. Singleton, R. D. Johnson, H. C. Walker, D. T. Adroja, A. D. Hillier, and A. A. Tsirlin, Phys. Rev. B **100**, 144432 (2019).
[36] J. Sichelschmidt, P. Schlender, B. Schmidt, M. Baenitz, and T. Doert, J. Phys.: Condens. Matter **31**, 205601 (2019).
[37] J. Sichelschmidt, B. Schmidt, P. Schlender, S. Khim, T. Doert, and M. Baenitz, in *Proceedings of the International Conference*

on Strongly Correlated Electron Systems (SCES2019), JPS Conference Proceedings Vol. 30 (Physical Society of Japan, Tokyo, 2020), p. 011096.
[38] Y.-T. Jia, C.-S. Gong, Y.-X. Liu, J.-F. Zhao, C. Dong, G.-Y. Dai, X.-D. Li, H.-C. Lei, R.-Z. Yu, G.-M. Zhang, and C.-Q. Jin, Chin. Phys. Lett. **37**, 097404 (2020).
[39] Y. Shimizu, T. Hiramatsu, M. Maesato, A. Otsuka, H. Yamochi, A. Ono, M. Itoh, M. Yoshida, M. Takigawa, Y. Yoshida, and G. Saito, Phys. Rev. Lett. **117**, 107203 (2016).
[40] Z. Zhu and S. R. White, Phys. Rev. B **92**, 041105(R) (2015).
[41] P. H. Y. Li, R. F. Bishop, and C. E. Campbell, Phys. Rev. B **91**, 014426 (2015).
[42] Y.-D. Li, X. Wang, and G. Chen, Phys. Rev. B **94**, 035107 (2016).
[43] Q. Luo, S. Hu, B. Xi, J. Zhao, and X. Wang, Phys. Rev. B **95**, 165110 (2017).
[44] J. S. Gardner, M. J. P. Gingras, and J. E. Greedan, Rev. Mod. Phys. **82**, 53 (2010).
[45] A. W. C. Wong, Z. Hao, and M. J. P. Gingras, Phys. Rev. B **88**, 144402 (2013).
[46] H. Yan, O. Benton, L. Jaubert, and N. Shannon, Phys. Rev. B **95**, 094422 (2017).
[47] J. D. M. Champion, M. J. Harris, P. C. W. Holdsworth, A. S. Wills, G. Balakrishnan, S. T. Bramwell, E. Čižmár, T. Fennell, J. S. Gardner, J. Lago, D. F. McMorrow, M. Orendáč, A. Orendáčová, D. McK. Paul, R. I. Smith, M. T. F. Telling, and A. Wildes, Phys. Rev. B **68**, 020401(R) (2003).
[48] J. Gaudet, A. M. Hallas, A. I. Kolesnikov, and B. D. Gaulin, Phys. Rev. B **97**, 024415 (2018).
[49] D. R. Yahne, L. D. Sanjeewa, A. S. Sefat, B. S. Stadelman, J. W. Kolis, S. Calder, and K. A. Ross, Phys. Rev. B **102**, 104423 (2020).
[50] Y. Cai, C. Lygouras, G. Thomas, M. N. Wilson, J. Beare, S. Sharma, C. A. Marjerrison, D. R. Yahne, K. A. Ross, Z. Gong, Y. J. Uemura, H. A. Dabkowska, and G. M. Luke, Phys. Rev. B **101**, 094432 (2020).
[51] Y. Cai, M. N. Wilson, J. Beare, C. Lygouras, G. Thomas, D. R. Yahne, K. Ross, K. M. Taddei, G. Sala, H. A. Dabkowska, A. A. Aczel, and G. M. Luke, Phys. Rev. B **100**, 184415 (2019).
[52] F. A. Cevallos, K. Stolze, and R. J. Cava, Solid State Commun. **276**, 5 (2018).
[53] J. Xing, L. D. Sanjeewa, J. Kim, W. R. Meier, A. F. May, Q. Zheng, R. Custelcean, G. R. Stewart, and A. S. Sefat, Phys. Rev. Materials **3**, 114413 (2019).
[54] J. Xing, K. M. Taddei, L. D. Sanjeewa, R. S. Fishman, M. Daum, M. Mourigal, C. dela Cruz, and A. S. Sefat, Phys. Rev. B **103**, 144413 (2021).
[55] S. Gao, F. Xiao, K. Kamazawa, K. Ikeuchi, D. Biner, K. W. Krämer, C. Rüegg, and T.-h. Arima, Phys. Rev. B **102**, 024424 (2020).
[56] W. Liu, D. Yan, Z. Zhang, J. Ji, Y. Shi, F. Jin, and Q. Zhang, Chin. Phys. B **30**, 107504 (2021).
[57] A. Scheie, V. O. Garlea, L. D. Sanjeewa, J. Xing, and A. S. Sefat, Phys. Rev. B **101**, 144432 (2020).
[58] L. Savary, K. A. Ross, B. D. Gaulin, J. P. C. Ruff, and L. Balents, Phys. Rev. Lett. **109**, 167201 (2012).
[59] G. Hester, T. N. DeLazzer, D. R. Yahne, C. L. Sarkis, H. D. Zhao, J. A. R. Rivera, S. Calder, and K. A. Ross, J. Phys.: Condens. Matter **33**, 405801 (2021).
[60] N. F. Chilton, R. P. Anderson, L. D. Turner, A. Soncini, and K. S. Murray, J. Comput. Chem. **34**, 1164 (2013).
[61] B. H. Toby, J. Appl. Crystallogr. **34**, 210 (2001).
[62] X. Z. Li, C. Wang, X. L. Chen, H. Li, L. S. Jia, L. Wu, Y. X. Du, and Y. P. Xu, Inorg. Chem. **43**, 8555 (2004).
[63] H. Cho, S. J. Blundell, T. Shiroka, K. MacFarquharson, D. Prabhakaran, and R. Coldea, arXiv:2104.01005.
[64] B. L. Pan, J. M. Ni, L. P. He, Y. J. Yu, Y. Xu, and S. Y. Li, Phys. Rev. B **103**, 104412 (2021).
[65] J. A. M. Paddison, M. Daum, Z. Dun, G. Ehlers, Y. Liu, M. B. Stone, H. Zhou, and M. Mourigal, Nat. Phys. **13**, 117 (2017).
[66] Z. Zhang, X. Ma, J. Li, G. Wang, D. T. Adroja, T. P. Perring, W. Liu, F. Jin, J. Ji, Y. Wang, Y. Kamiya, X. Wang, J. Ma, and Q. Zhang, Phys. Rev. B **103**, 035144 (2021).
[67] S. Guo, A. Ghasemi, C. L. Broholm, and R. J. Cava, Phys. Rev. Materials **3**, 094404 (2019).
[68] S. Guo, R. Zhong, K. Górnicka, T. Klimczuk, and R. J. Cava, Chem. Mater. **32**, 10670 (2020).
[69] K. W. H. Stevens, Proc. Phys. Soc. A **65**, 209 (1952).
[70] J. Kim, X. Wang, F.-T. Huang, Y. Wang, X. Fang, X. Luo, Y. Li, M. Wu, S. Mori, D. Kwok, E. D. Mun, V. S. Zapf, and S.-W. Cheong, Phys. Rev. X **9**, 031005 (2019).
[71] L. Ortega-San Martin, J. P. Chapman, L. Lezama, J. Sánchez Marcos, J. Rodríguez-Fernández, M. I. Arriortua, and T. Rojo, Eur. J. Inorg. Chem. **2006**, 1362 (2006).
[72] Q. J. Li, Z. Y. Zhao, H. D. Zhou, W. P. Ke, X. M. Wang, C. Fan, X. G. Liu, L. M. Chen, X. Zhao, and X. F. Sun, Phys. Rev. B **85**, 174438 (2012).
[73] W. Liu, Z. Zhang, D. Yan, J. Li, Z. Zhang, J. Ji, F. Jin, Y. Shi, and Q. Zhang, arXiv:2108.09693.
[74] M. J. P. Gingras, B. C. den Hertog, M. Faucher, J. S. Gardner, S. R. Dunsiger, L. J. Chang, B. D. Gaulin, N. P. Raju, and J. E. Greedan, Phys. Rev. B **62**, 6496 (2000).
[75] J. Xing, L. D. Sanjeewa, J. Kim, G. R. Stewart, M.-H. Du, F. A. Reboredo, R. Custelcean, and A. S. Sefat, ACS Mater. Lett. **2**, 71 (2020).
[76] R. Bag, M. Ennis, C. Liu, S. E. Dissanayake, Z. Shi, J. Liu, L. Balents, and S. Haravifard, Phys. Rev. B **104**, L220403 (2021).
[77] B. C. den Hertog and M. J. P. Gingras, Phys. Rev. Lett. **84**, 3430 (2000).
[78] S. Onoda and Y. Tanaka, Phys. Rev. B **83**, 094411 (2011).
[79] Y. J. Uemura, A. Keren, K. Kojima, L. P. Le, G. M. Luke, W. D. Wu, Y. Ajiro, T. Asano, Y. Kuriyama, M. Mekata, H. Kikuchi, and K. Kakurai, Phys. Rev. Lett. **73**, 3306 (1994).
[80] J. G. Rau and M. J. P. Gingras, Phys. Rev. B **98**, 054408 (2018).
[81] A. M. Hallas, J. Gaudet, and B. D. Gaulin, Annu. Rev. Condens. Matter Phys. **9**, 105 (2018).
[82] L. S. Wu, S. E. Nikitin, M. Brando, L. Vasylechko, G. Ehlers, M. Frontzek, A. T. Savici, G. Sala, A. D. Christianson, M. D. Lumsden, and A. Podlesnyak, Phys. Rev. B **99**, 195117 (2019).